# Effects of Tunable Hydrophobicity on the Collective Hydrodynamics of Janus Particles under Flows

Szu-Pei Fu[1], Rolf Ryham[2], Bryan Quaife[3] and Y.-N. Young[4]

[1]*Department of Mathematics, Trinity College, Hartford, Connecticut 06106, USA*

[2]*Department of Mathematics, Fordham University, Bronx, New York 10458, USA*

[3]*Department of Scientific Computing, Florida State University, Tallahassee, Florida 32306, USA*

[4]*Department of Mathematical Sciences, New Jersey Institute of Technology, Newark, New Jersey 07102, USA*

(Dated: April 25, 2023)

## Abstract

Active colloidal systems with non-equilibrium self-organization is a long-standing, challenging area in material sciences and biology. To understand how hydrodynamic flow may be used to actively control self-assembly of Janus particles (JPs), we developed a model for the many-body hydrodynamics of amphiphilic JPs suspended in a viscous fluid with imposed far-field background flows (Journal of Fluid Mechanics, 941, 2022). In this work we alter the hydrophobic distribution on the JP-solvent interface to investigate the hydrodynamics that underlies the various morphologies and rheological properties of the JP assembly in the suspension. We find JPs assemble into unilamellar, multilamellar, and striated structures. To introduce dynamics, we include a planar linear shear flow and a steady Taylor-Green mixing flow, and measure the collective dynamics of JP particles in terms of their (a) free energy from the hydrophobic interactions between the JPs, (b) order parameter for the ordering of JPs in terms of alignment of their directors, and (c) strain parameter that captures the deformation in the assembly. We characterize the effective material properties of the JP structures and find that the unilamellar structures increases orientation order under shear flow, the multilamellar structure behaves as a shear thinning fluid, and the striated structure possesses a yield stress. These numerical results provide insights into dynamic control of non-equilibrium active biological systems with similar self-organization.

## I. INTRODUCTION

Janus particles (JPs) are colloids with dissimilar chemical or physical functionalities between the two sides of their surfaces [1, 2]. Self-propelling JPs, for example, with a permanent biphasic asymmetry, have emerged as a rich chemical platform for the exploration of active matter [3] and mobility induced phase separation. In the absence of mobility and any imposed flow, JPs self-assemble into oligomers of various geometries and sizes depending on the interactions between JPs and the viscous solvent [4–6], with tunable functions for biomedical engineering applications [2, 7–11].

When driven by an external flow, dynamic rearrangement of JPs emerges naturally from the interactions between particles and fluid in colloidal matter [12]. Such colloidal hydrodynamics belong to a wide class of nonequilibrium self-organization in physics, often with complexity and features similar to that of biological systems such as living cells, bacterial baths, and animal flocks [13, 14]. A long-standing challenge in fluid mechanics and material science is to solve the "inverse" problem of creating a model colloidal system that will self-assemble into prescribed structures [15]. For example, the framework of geometrical frustration, which has been used to explain disordered systems, could instead be used to design new, ordered systems, through specific choices for the shapes or interactions of the particles [16].

In this work we focus on collective hydrodynamics of immobile (non self-propelling) JPs in a viscous fluid under an imposed far-field flow. The amphiphilic JP has a hydrophobic surface on one side and a hydrophilic surface on the other side [17]. The many-body hydrodynamics of amphiphilic Janus particles assembled as vesicles (self-enclosed bilayers of JPs) suspended in a viscous fluid in the inertialess regime (zero Reynolds number) has been studied using boundary integral numerical simulations [18, 19]. The dynamics of the JP suspension arises spontaneously from the combination of long-range hydrodynamic interaction and non-local interactions between JPs through the distribution of a hydrophobic attraction potential (HAP). In a quiescent flow, an amphiphilic JP suspension self-assembles into micelles and bilayers of JPs that provide an alternative means for computing the mechanical moduli of a colloidal membrane in numerical simulations [18, 20, 21]. Under background flows, the hydrodynamics of a JP vesicle (a self-enclosed bilayer of JPs) exhibit many familiar behaviors of a vesicle: elongation and alignment along the extensional direction, tank-treading, and rupture of a vesicle under shear flow [19, 22–26].

Molecular dynamics (MD) and Monte Carlo simulations provide another means for simulating the interaction between amphiphilic JPs, solvents, and substrates [6, 27–29]. In these methods pair-potentials are used to describe the interaction between amphiphilic JPs by prescribing angle dependent forces and torques that bring the hydrophobic sides of two amphiphilic JPs into opposition. On the other hand, the HAP formulation of the present work has attractive, long-range forces and torques, and they are instead derived from a boundary value problem for the molecular structure of water [30–34]. Unlike in MD or Monte Carlo simulations, the HAP interactions are nonadditive [18], so that the interactions between a pair of JPs is affected by the presence of other particles. As such, the HAP is a phase-field function that represents the properties of the solvent in the presence of JPs. Such approach falls into the category of work that considers particles as a discretization of a continuum problem [35].

Here we take advantage of the flexibility of the HAP model to examine the effects of tuning the distribution of hydrophobicity on JP surfaces. Such variation of the boundary condition on JP surfaces has been realized experimentally by using chemicals to adjust the polarity of the viscous solvent [2, 11, 17]. We show that a simple tuning of the hydrophobic distribution leads to transitions from unilamellar to multilamellar or striated superstructures of JPs. Focusing on the fluid-structure interactions that correspond to such transitions, we investigate the deformation of these novel structures in background flows and map out their collective behavior away from equilibrium. Looking forward, including other fields like electric potential for JPs synthesized with charged polymers [5, 6, 17], is straightforward within the context of the boundary integral representations [36], opening further lines of investigation.

This paper is organized as follows. § II summarizes the general mathematical formulation. § III describes the three types of hydrophobicity distribution that we use in the numerical simulations. § IV outlines the quantitative measures used to describe the collective hydrodynamics of JPs summarized and discussed in § IV. Finally, § VI provides a conclusion and discussion for future directions.

## II. GOVERNING EQUATIONS: HYDROPHOBIC ATTRACTION POTENTIAL MOBILITY PROBLEM

The governing equations are a system of partial differential equations for the position and orientation of a collection of rigid JPs [19]. We first pose the Stokes equations for the mobility problem giving the hydrodynamic interactions for the particle suspension. The hydrophobic forces come from solving a screened Laplace equation. Particle collisions are avoided through a near-field, pair potential for their steric interactions.

### A. Mobility problem

The JPs are disks of radius $c$ suspended in a viscous solvent with center $\mathbf{a}_i$, and orientation $\theta_i$ relative to the horizontal axis, where $i = 1, \ldots, N_b$, and $N_b$ is the number of particles. The domain $\Omega \subset \mathbb{R}^2$ is the solvent phase and $t$ is time. The boundary of $\Omega$ is $\partial\Omega = \Gamma_1 \cup \cdots \cup \Gamma_{N_b}$, where $\Gamma_i$ is the boundary of Janus particle $i$. The sets $\Omega$, $\Gamma_1, \ldots,$ and $\Gamma_{N_b}$ depend on $t$. Assuming inertial terms are negligible, the solvent satisfies the Stokes equations

$$-\mu\Delta\mathbf{u} + \nabla p = \mathbf{0}, \qquad \mathbf{x} \in \Omega, \tag{1}$$

$$\nabla \cdot \mathbf{u} = 0, \qquad \mathbf{x} \in \Omega, \tag{2}$$

$$\mathbf{u} - \mathbf{u}_\infty \to \mathbf{0}, \qquad |\mathbf{x}| \to \infty, \tag{3}$$

where $\mathbf{u}$ is the velocity, $p$ is the pressure, $\mathbf{u}_\infty$ is the background flow velocity, and $\mu$ is the constant solvent viscosity. The solvent velocity satisfies the no-slip boundary condition for a rigid body motion

$$\mathbf{u}(\mathbf{x}) = \mathbf{v}_i + \omega_i(\mathbf{x} - \mathbf{a}_i)^\perp, \quad \mathbf{x} \in \Gamma_i, \tag{4}$$

where $\mathbf{v}_i$ is the translational velocity, $\omega_i$ is the angular velocity, and $\langle x, y\rangle^\perp = \langle -y, x\rangle$.

To obtain forces, define the free energy [18, 19]

$$F = \gamma \int_\Omega \left(\rho|\nabla u|^2 + \rho^{-1}u^2\right) d\mathbf{x} + \frac{M}{2}\sum_{j\neq i} P\left(\frac{|\mathbf{a}_i - \mathbf{a}_j| - 2c}{\rho_0}\right), \tag{5}$$

where $u(\mathbf{x}, t)$ is as the order parameter for water [30, 31], $\rho$ is a decay length, and $\gamma$ is an interfacial tension. The order parameter $u(\mathbf{x}, t)$ is assumed to minimize the free energy $F$ and therefore satisfies the screened Laplace boundary value problem

$$-\rho^2\Delta u + u = 0, \quad \mathbf{x} \in \Omega, \tag{6}$$

$$u = g, \quad \mathbf{x} \in \partial\Omega, \quad u \to 0, \quad |\mathbf{x}| \to \infty. \tag{7}$$

The boundary condition $g$ encodes hydrophobic properties of the particle-solvent interface. The dimensionless repulsion profile takes the form $P(s) = 1 - \sin(\pi s/2)$ for $0 \leq s < 1$ and $P(s) = 0$ for $s \geq 1$. The parameter $\rho_0$ is the distance below which steric repulsion becomes important and $M$ is the repulsion modulus.

Letting $\boldsymbol{\nu}$ be the particle outward normal, the force $\mathbf{F}_i$ and torque $T_i$ coming from the free energy acting on $\Gamma_i$ are [18]

$$\mathbf{F}_i = \int_{\Gamma_i} \mathbf{T}\boldsymbol{\nu}\ \mathrm{d}s - \frac{M}{\rho_0}\sum_{j\neq i}\frac{\mathbf{a}_i - \mathbf{a}_j}{|\mathbf{a}_i - \mathbf{a}_j|}P'\left(\frac{|\mathbf{a}_i - \mathbf{a}_j| - 2c}{\rho_0}\right), \quad T_i = \int_{\Gamma_i}(\mathbf{x} - \mathbf{a}_i)^\perp \cdot (\mathbf{T}\boldsymbol{\nu})\ \mathrm{d}s. \tag{8}$$

Here,

$$\mathbf{T} = \gamma\left[\rho^{-1}u^2\mathbf{I} + \rho\left(|\nabla u|^2\mathbf{I} - 2\nabla u\nabla u^T\right)\right] \tag{9}$$

is the second-order hydrophobic stress tensor. Repulsion is rotationally symmetric and does not enter $T_i$.

Without inertia, $(\mathbf{u}, p)$ satisfy the force-free and torque-free conditions, meaning that the force and torque from the hydrodynamic stress on each particle balance the total force and torque coming from the hydrophobic potential and repulsion. We have

$$\int_{\Gamma_i} \boldsymbol{\sigma}\cdot\boldsymbol{\nu}\ \mathrm{d}s = \mathbf{F}_i, \quad \int_{\Gamma_i}(\mathbf{x} - \mathbf{a}_i)^\perp \cdot (\boldsymbol{\sigma}\cdot\boldsymbol{\nu})\ \mathrm{d}s = T_i, \quad i = 1, \ldots, N_b, \tag{10}$$

where $\boldsymbol{\sigma} = -p\mathbf{I} + \mu\left(\nabla\mathbf{u} + \nabla\mathbf{u}^T\right)$ is the hydrodynamic stress tensor.

To perform a single time step, we (i) solve (6)–(7) for $u$, (ii) compute the force and torque (8), and (iii) solve the Stokes equations (1)–(3) subject to (4) and (10). The velocities $(\mathbf{v}_i, \omega_i)$ obtained from (4) are used to update the particle positions and orientations using the second-order Adams-Bashforth scheme with time step size $\Delta t$.

The interactions generated by the HAP-mobility problem formulation (1)–(10) lead to particle self-assembly. In terms of scaling, $\rho$ sets the effective distance of the hydrophobic interactions; $\rho_0$ determines the distance where attraction and repulsion are in balance i.e. smaller values of $\rho_0$ lead to more compact particle assemblies. The rate of self-assembly is proportional to tension $\gamma$, inversely proportional to viscosity $\mu$, and approximately inversely proportional to $\rho$ [18].

### B. Boundary integral representations

We require a method to accurately solve the Stokes and screened Laplace equations in intricate, unbounded geometries. This is done by recasting (1)–(4) and (6)–(7) as boundary integral equations (BIEs) and discretizing each BIE at $N$ points on each of the $N_b$ particles with a collocation method. To express the solution of (6)–(7), we adopt the double-layer potential

$$u(\mathbf{x}) = \mathcal{D}[\sigma](\mathbf{x}) = \int_{\partial\Omega} \frac{\partial G(\mathbf{x}-\mathbf{y})}{\partial \boldsymbol{\nu}_{\mathbf{y}}} \eta(\mathbf{y})\, \mathrm{d}s_{\mathbf{y}}, \quad \mathbf{x} \in \Omega, \tag{11}$$

where $G(\mathbf{x}) = \frac{1}{2\pi} K_0(|\mathbf{x}|/\rho)$ is the fundamental solution of the screened Laplace equation (6), $K_0$ is the zeroth-order modified Bessel function of the second kind, $\boldsymbol{\nu}_{\mathbf{y}}$ is the unit outward normal at $\mathbf{y}$, and $\eta$ is a scalar-valued density function. The subscript in $\mathrm{d}s_{\mathbf{y}}$ denotes integration with respect to $\mathbf{y} \in \partial\Omega$. To satisfy the boundary condition (7), the density function must satisfy [37]

$$g(\mathbf{x}) = \frac{1}{2}\eta(\mathbf{x}) + \mathcal{D}[\eta](\mathbf{x}), \quad \mathbf{x} \in \partial\Omega. \tag{12}$$

For the velocity, we use the completed double-layer potential representation [38]

$$\mathbf{u}(\mathbf{x}) = \mathbf{u}_\infty(\mathbf{x}) + \mathcal{D}[\boldsymbol{\eta}](\mathbf{x}) + \sum_{i=1}^{N_b} \left(\mathbf{S}(\mathbf{x}, \mathbf{a}_i) \cdot \mathbf{F}_i + \mathbf{R}(\mathbf{x}, \mathbf{a}_i) T_i\right), \quad \mathbf{x} \in \Omega, \tag{13}$$

where $\boldsymbol{\eta}$ is a vector-valued density function and

$$\mathcal{D}[\boldsymbol{\eta}](\mathbf{x}) = \frac{1}{\pi} \int_{\Gamma} \frac{(\mathbf{x}-\mathbf{y}) \cdot \boldsymbol{\nu}_{\mathbf{y}}}{|\mathbf{x}-\mathbf{y}|^2} \frac{(\mathbf{x}-\mathbf{y}) \otimes (\mathbf{x}-\mathbf{y})}{|\mathbf{x}-\mathbf{y}|^2} \cdot \boldsymbol{\eta}(\mathbf{y})\, \mathrm{d}s_{\mathbf{y}}. \tag{14}$$

The Stokeslets and Rotlets are

$$\mathbf{S}(\mathbf{x}, \mathbf{a}_i) = \frac{1}{4\pi}\left(-\log|\mathbf{r}|\mathbf{I} + \frac{\mathbf{r}\otimes\mathbf{r}}{|\mathbf{r}|^2}\right), \quad \mathbf{R}(\mathbf{x}, \mathbf{a}_i) = \frac{1}{4\pi}\frac{\mathbf{r}^\perp}{|\mathbf{r}|^2}, \tag{15}$$

respectively, where $\mathbf{r} = \mathbf{x} - \mathbf{a}_i$. Letting $\mathbf{x}$ approach $\Gamma_i$ in (13), applying the jump condition of the double layer potential [39], and imposing the no-slip boundary condition (4), the density function $\boldsymbol{\eta}$, translational velocity $\mathbf{v}_i$, and rotational velocity $\omega_i$ satisfy

$$\mathbf{v}_i + \omega_i(\mathbf{x} - \mathbf{a}_i)^\perp = \mathbf{u}_\infty(\mathbf{x}) - \frac{1}{2}\boldsymbol{\eta}(\mathbf{x}) + \mathcal{D}[\boldsymbol{\eta}](\mathbf{x}) + \sum_{j=1}^{N_b}\left(\mathbf{S}(\mathbf{x}, \mathbf{a}_j)\cdot\mathbf{F}_j + \mathbf{R}(\mathbf{x}, \mathbf{a}_j)T_j\right), \tag{16}$$

$$\int_{\Gamma_i}\boldsymbol{\eta}\,\mathrm{d}s = \mathbf{F}_i, \quad \int_{\Gamma_i}\boldsymbol{\eta}\cdot(\mathbf{x} - \mathbf{a}_i)^\perp\,\mathrm{d}s = T_i, \tag{17}$$

for $\mathbf{x} \in \Gamma_i$ and $i = 1, \ldots, N_b$. Alternative full-rank layer potential representations for rigid body motions are possible [40, 41].

We discretize (12) and (16)–(17) using high-order interpolation-based quadrature rules. Smooth integrals are computed with the spectrally-accurate trapezoid rule, and nearly-singular integrals, caused by close contact between two particles, are computed with a high-order interpolation-based quadrature rule [42].

After discretizing and applying quadrature, the result is an $NN_b \times NN_b$ and $(2N+3)N_b \times (2N+3)N_b$ linear system for (12) and (16)–(17), respectively. These are solved with matrix-free GMRES and the second-kind nature of the BIEs guarantees that the number of GMRES iterations is mesh-independent.

## III. TUNABLE HYDROPHOBICITY

The parameters are modeled after those for phospholipid in water [43]. We use $\mu = 1$ mPa s for the viscosity of water at room temperature. Pure lipid components give a range of interfacial tensions [44–47]; 0.7–5.3 pN nm$^{-1}$. We use $\gamma = 4.1$ pN nm$^{-1}$ which gives a physically reasonable elastic modulus $\kappa$ of lipid bilayers [18, 19]. The particle radius $c = 1.25$ nm represents one half of phospholipid length [43], and the screening length $\rho = 5$ nm derives from experimental force-distance measurements of hydrophobic attraction [32–34, 46]. A repulsion modulus $M = 2$ pN and distance $\rho_0 = 0.5$ nm gives an interparticle distance around one particle radius, ensuring the accuracy of the boundary integral representations (11) and (13) without overly aggressive mesh refinement. The characteristic time and length are 1 ns and 1 nm, respectively.

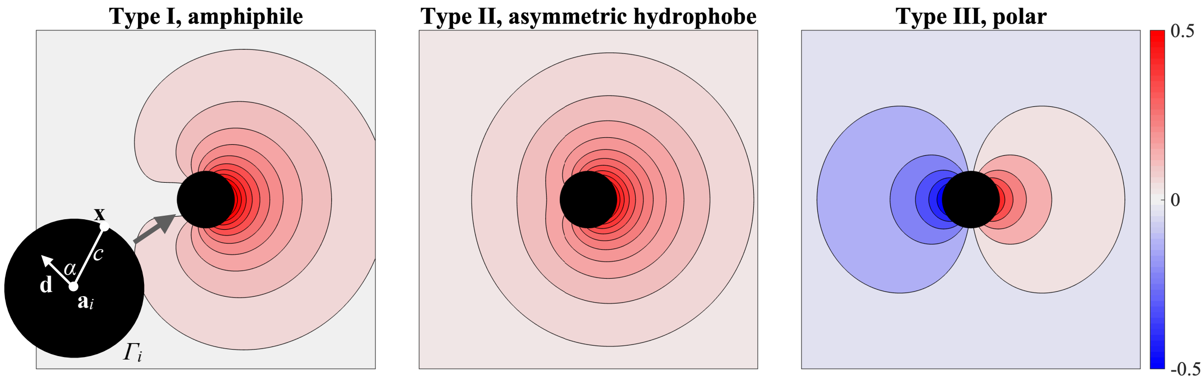


FIG. 1. The leftmost diagram illustrates the particle $\Gamma_i$ with center $\mathbf{a}_i$, radius $c$, and director $\mathbf{d}$, along with the angle $\alpha$. The three rightmost panels plots show $g(\mathbf{x})$ and the respective solutions $u(\mathbf{x})$ of (6) for an isolated particle.

### A. Boundary conditions and equilibrium configurations

The boundary condition $g(\mathbf{x})$ in (7) defines the spatial distribution of hydrophobicity and hydrophilicity. Referring to Figure 1, we let

$$g(\mathbf{x}) = a(b + \cos\alpha), \quad a = (\pi c(2b^2 + 1))^{-1/2}, \quad \mathbf{x} \in \Gamma_i, \tag{18}$$

where $\alpha$ is the angle between the vector $\mathbf{x} - \mathbf{a}_i$ and the particle director $\mathbf{d}_i = (\cos\theta_i, \sin\theta_i)$. The scalar $b$ shifts the periodic date up and down and the scalar $a$ normalizes $g$ so that $\int_{\Gamma_i} g^2(\mathbf{x})\, \mathrm{d}s = 1$. The side of the particle where $\alpha = 0$ is called the tail and the side where $\alpha = \pi$ is the head.

Based on the choice of $b$, the boundary condition (BC) (18) can be classified into one of three categories: Type I, amphiphile, $b = 1$, $g$ is positive on one side representing a hydrocarbon-water interface, and is zero on the other representing an apolar, hydrophilic region; Type II, asymmetric hydrophobe, $b = 2$, $g$ is positive on both sides but more so on one side; Type III, polar, $b = 0$, $g$ is positive on one side and negative on the other, representing a water structure with positive/negative charge [30, 48].

Figure 2 shows the steady state in a quiescent flow. Three distinct phases emerge. For Type I, amphiphiles, the tail interactions are attractive, and particles collectively form disjoint bilayer components (Figure 2(b)). We refer to this as the "bilayer" phase.

For Type II, asymmetric hydrophobes, both sides of the JP are hydrophobic but more so on the tail. Over short times, these particles self-assemble into bilayers. But unlike for Type I JPs,

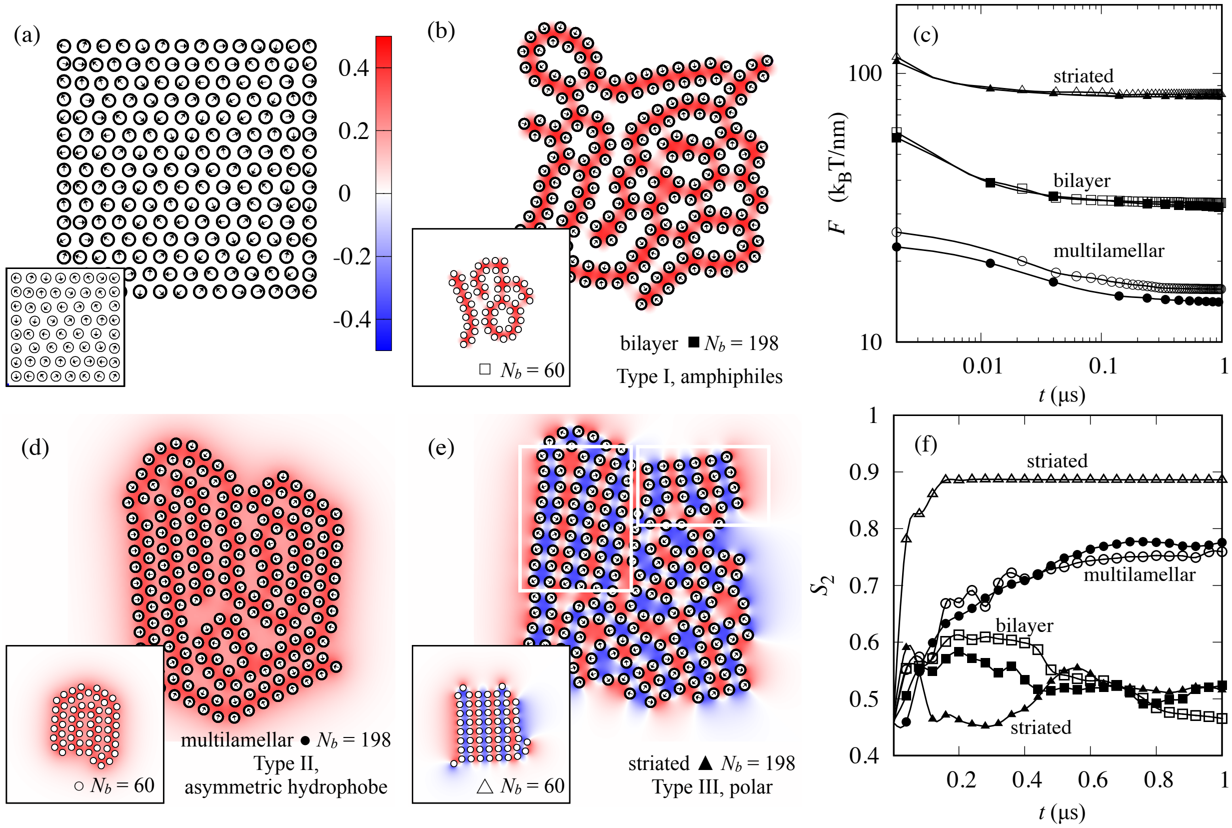


FIG. 2. Panel (a) shows the $t = 0$, $N_b = 198$ particle configuration with random orientation and initially confined to a box. Panels (b), (d), (e) show bilayer, multilamellar, and striated phases composed of amphiphilic (Type I), asymmetric hydrophobe (Type II), and polar (Type III) JP, respectively. Panels (c) and (f) plot the free energies (5) and alignment order parameter (22) with respect to $t$. The open markers in panel (c) are for $N_b = 60$ and the solid markers are for $N_b = 198$ but normalized by $60/198$, showing that the energy approximately scales with the number of particles. Alignment in the striated phase is particle-number dependent; triangle markers, panel (f).

the heads are also hydrophobic and so over long times, the bilayers sort into a "multilamellar" phase. The number of layers depends on the number of particles. Figure 2(d), for example, shows a multilamellar structure with four layers and one with two layers in the inset. Onion-like dendrimersomes have previously been studied by molecular dynamics simulations using an anisotropic pair potential [6, 29].

Finally, Type III, bipolar JPs possess a head that repels the tail of neighboring particles. These JP initially form chains with their directors perpendicular to the length of the chain. The chains form stria where the particles lie on a square grid and the orientations alternate between layers (Figure 2(e)). We refer to this as the "striated" phase.

See Section S1 in the Supplementary Material for movies showing the transition of 60 JPs that are initialized randomly (inset of Figure 2(a)) to the steady state configurations (inset of Figures 2(b), (d), and (e)) [49].

## IV. MEASURING DEFORMATION

To quantify the hydrodynamics of JP phases, we use the free energy $F$, a strain parameter $E$, and a scalar order parameters $S_2$ for alignment. First we simplify the form of the free energy (5). Using integration by parts and (6), we obtain

$$F = -\gamma \int_{\partial\Omega} \rho g \nabla u \cdot \boldsymbol{\nu} \, \mathrm{d}s + \frac{M}{2} \sum_{j \neq i} P\left(\frac{|\mathbf{a}_i - \mathbf{a}_j| - 2c}{\rho_0}\right). \tag{19}$$

Here, we have substituted $g$ for $u$ since the boundary values are given. However, evaluating $\nabla u \cdot \boldsymbol{\nu}$ on $\partial\Omega$ based on (11) involves calculating a gradient of a double-layer potential which has a well-known obstacle in numerical implementation. Appendix VII describes how we overcome this obstacle.

Figure 2(c) tracks the free energy profiles for all relaxation runs. In quiescent background flow, the energies are decreasing with respect to $t$ showing time stepping correctly accounts for viscous dissipation. Furthermore, the normalized energy plots provide evidence that the free energy per particle with specified boundary condition is independent of the total particle number ($N_b$).

To measure positional order, we introduce the strain parameter,

$$E = \frac{1}{N_b} \sum_{i=1}^{N_b} \left\| \tfrac{1}{2}(\mathsf{F}_i^T \mathsf{F}_i - I) \right\|, \tag{20}$$

where $\mathsf{F}_i$ is an approximate deformation gradient and $\|\cdot\|$ is the Frobenius norm. The Green-Lagrange strain tensor $\frac{1}{2}(\mathsf{F}_i^T \mathsf{F}_i - I)$ measures departure of fluid deformations from a rigid body motion. To define $\mathsf{F}_i$, we solve the overdetermined system

$$\mathbf{a}_j(t) - \mathbf{a}_i(t) = \mathsf{F}_i(\mathbf{a}_j(0) - \mathbf{a}_i(0)), \quad j = 1, \ldots, N_b, \tag{21}$$

for $\mathsf{F}_i$ by weighted least squares. That way, if the particle positions are given by a map $\mathbf{f}(\mathbf{a}_i(0), t) = \mathbf{a}_i(t)$, then $\mathsf{F}_i \approx \nabla \mathbf{f}(\mathbf{a}_i(0), t)$. The weights $w_i = \exp(-\|\mathbf{a}_j(0) - \mathbf{a}_i(0)\|/4c)$ with particle radius $c$ ensure that the linear approximation holds for particles near $\mathbf{a}_i$.

Finally, we use the scalar order parameter $S_2$ to quantify the orientational order [50]:

$$S_2 = \frac{1}{N_b} \sum_{i=1}^{N_b} \frac{1}{2} (3\cos^2(\theta_i - \bar{\theta}) - 1). \tag{22}$$

Here $\bar{\theta}_i$ is a circular mean defined as the orientation of the principal eigenvector of the matrix $\sum_j \mathbf{d}_j \mathbf{d}_j^\top$ where $j$ runs over the particles whose centers lie with $4c$ of that of particle $i$. Defined as such, $S_2$ lies in the range $-1/2 \leq S_2 \leq 1$ with a value $S_2 = 1$ indicating perfect alignment between particles while $S_2 = -1/2$ indicating isotropic alignment locally. The cutoff distance $4c$ was chosen empirically so that the average includes nearest neighbors but excludes next nearest neighbors.

In Figure 2(f), the multilamellar phase is highly ordered whereas the bilayer phase is somewhat disordered because it consists of several components forming isolated bilayers, micelles, and vesicles (Figure 2(b)).

The striated phase order admits more than one pattern depending on the number of particles (Figure 2(f), triangles). When the number of particles is fewer, there is only a single pattern where the directors are more or less parallel and alternate directions (Figure 2(e), inset). Larger number of particles results in multiple alignment patterns: the alternating sign pattern as in the small particle number case (Figure 2(e), top right rectangle) and an 'X'-shaped alignment (Figure 2(e), top left rectangle).

## V. RESULTS AND DISCUSSION

We subject the Type I, II, and III JP phases to background flows and measure their material response. The background flows are a shear flow

$$\mathbf{u}_\infty^{\text{sh}}(\mathbf{x}) = \dot{\gamma}(\mathbf{e}_y \cdot \mathbf{x})\mathbf{e}_x, \tag{23}$$

and a Taylor-Green (TG) flow

$$\mathbf{u}_\infty^{\text{TG}}(\mathbf{x}) = \lambda\dot{\gamma} \left(-\cos(\mathbf{e}_x \cdot \mathbf{x}/\lambda) \sin(\mathbf{e}_y \cdot \mathbf{x}/\lambda)\mathbf{e}_x + \sin(\mathbf{e}_x \cdot \mathbf{x}/\lambda) \cos(\mathbf{e}_y \cdot \mathbf{x}/\lambda)\mathbf{e}_y\right), \tag{24}$$

where the orthonormal vectors $\mathbf{e}_x$ and $\mathbf{e}_y$ are the horizontal and vertical directions, respectively. The shear flow replicates the motion of a fluid between two parallel, moving plates excluding wall effects. In TG flow, $\lambda$ controls the size of the $\pi\lambda \times \pi\lambda$ TG cells. Throughout this section, we use $\lambda = 2$ nm so that the JP phases occupy about nine cells.

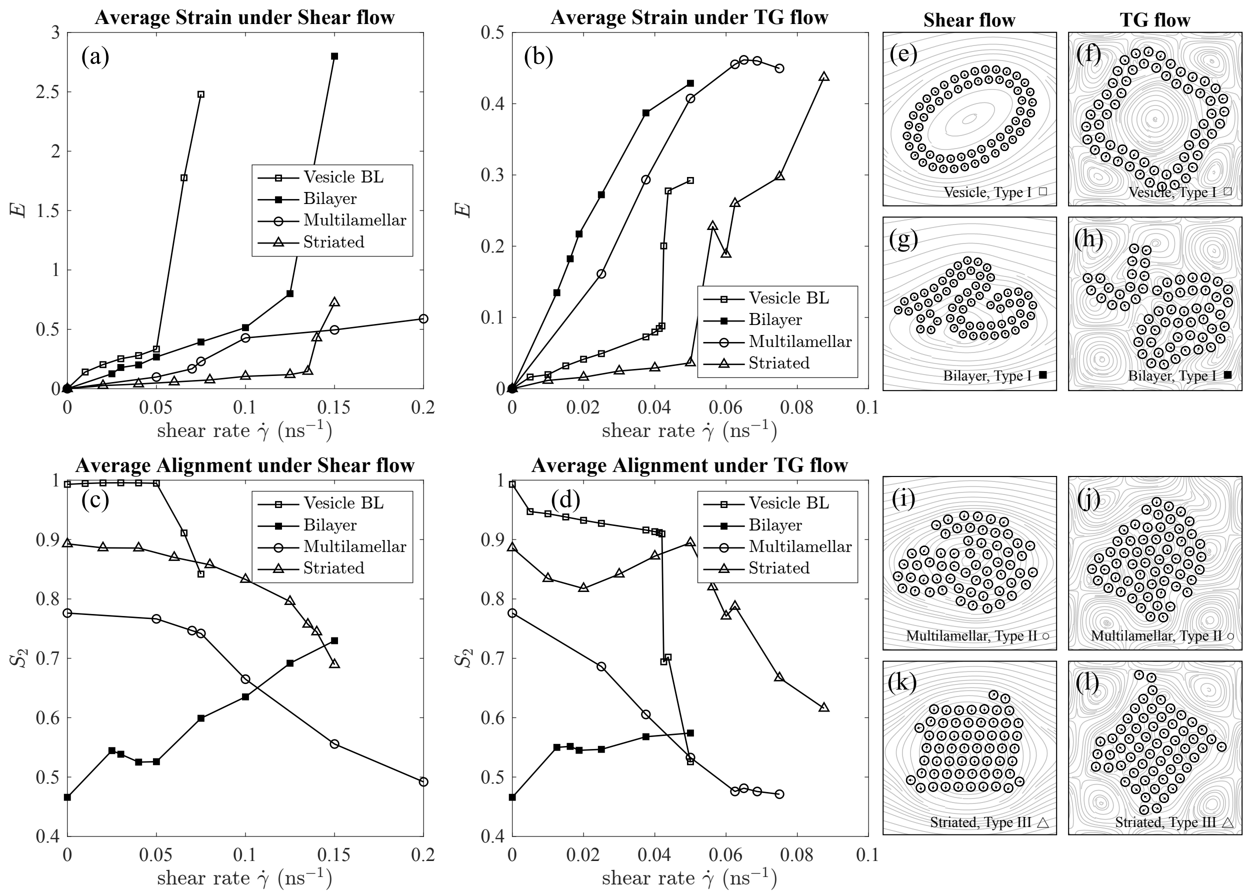


FIG. 3. Panel (a)–(b) show the average strain increase for bilayer, vesicle BL, multilamellar, and striated JP structures under a shear flow and a TG flow, respectively. Panel (c)–(d) show the average alignment of four JP structures under a shear flow and a TG flow, respectively. Each snapshot of panels (e)–(l) contains the configurations of the JP structure without ruptures using a specific type of boundary condition and the background curves indicate the velocity streamlines.

In both cases, $\dot{\gamma}$ is the shear rate. The flow rate $\lambda\dot{\gamma}$ is chosen so that (24) has the same rate of viscous dissipation per area as for (23). In other words, $\int_A \frac{1}{2}\mu|\nabla\mathbf{u} + \nabla\mathbf{u}^T|^2 \, \mathrm{d}A$ is the same for $\mathbf{u} = \mathbf{u}_\infty^{\mathrm{sh}}$ as for $\mathbf{u} = \mathbf{u}_\infty^{\mathrm{TG}}$ when integrated over a TG cell $A$.

To obtain a range for $\dot{\gamma}$, consider the capillary number

$$\mathrm{Ca} = \frac{\mu\dot{\gamma}R^3}{\kappa} \tag{25}$$

where $R = 10$ nm and $\kappa = 20\ \mathrm{k_B T}$ are the characteristic phase sample radius and bending rigidity, respectively. That is, $\kappa$ gives the elastic stress for restoring the phase-sample shape. Shear stress overcomes elastic stress when $\mathrm{Ca} > 1$ and this yields $\dot{\gamma} > 2\cdot 10^{-2}\ \mathrm{ns}^{-1} = 2\cdot 10^{6}\ \mathrm{s}^{-1}$. Thus our values for $\dot{\gamma}$ range between 0 $\text{ns}^{-1}$ corresponding to quiescent flow up to 0.2 $\text{ns}^{-1}$ capable of rupturing the sample. Such shear rates are compatible with molecular dynamics simulation [27], those for large unilamellar vesicles (LUV), [51], and shearing in blood capillary vessels [52] where shear rates range over 100–2000 $\text{s}^{-1}$. From the particle diffusion time $D/L^2$ and advection time $L/u = (\dot{\gamma})^{-1}$, $D = 0.17 \cdot 10^{-9}$ $\text{m}^2$ $\text{s}^{-1}$ and $L \sim 10$ nm, we obtain a Péclet number $\text{Pe} = (D/L^2)/(L/u) \sim 60$, suggesting that advection dominates the particle transport.

For initial data, note that the steady-state Type I amphiphiles phase consists of a number of disjoint bilayer components (Figure 2(b)). To also have a single-component Type I phase, we reinitialize the data to have a ring-shaped vesicle bilayer. This phase is distinguished from "bilayer" by "vesicle BL" in the figures. For the same number of JP, the vesicle bilayer has lower free steady-state energy ($F = 24.6$ $\text{k}_\text{B}\text{T}$ $\text{nm}^{-1}$) than the disordered bilayer phase ($F = 27.2$ $\text{k}_\text{B}\text{T}$ $\text{nm}^{-1}$). Since the simulations are for two dimensions, multiplying $F$ by a length gives the energy of a transversely invariant, three-dimensional phase.

The simulation setup consists of placing each of the phases in either a shear or TG background flow and then solving for the particle trajectories in time. In each setup, we solved for 500 time steps with $\Delta t = 2$ ns, yielding time courses for $t \in [0, T]$, $T = 1$ μs. We then post-process the trajectories.

Figure 3(e)–(l) show the typical streamlines for JP phases in background flow. Although the plots only show the region near the JPs, the fluid velocity $\mathbf{u}$ and order parameter $u$ are accounted for in all of $\mathbb{R}^2$. Moreover, $\mathbf{u}$ satisfies the rigid boundary condition at every JP-fluid interface i.e., the particles interact with the local flow field and are not merely carried by background flow. See Section S1 in the Supplementary Material for movies showing the dynamics of the JP suspensions in Figure 3 [49].

Figures S1–S8 in the Supplementary Material contain the fully-resolved time courses for the free energy $F$, alignment order $S_2$, and strain $E$ [49]. The eight setups correspond to the four JP phases—bilayer, vesicle BL, multilamellar, and striated—and two background flows—shear and TG, and the data are plotted with the same vertical and horizontal axes to facilitate comparisons between simulation setups. Each setup considers a range of shear rates $\dot{\gamma}$ in the interval $[0, 0.2]$ $\text{ns}^{-1}$.

The fully-resolved time courses in Figures S1–S8 in the Supplementary Material contain significant oscillations due to the particle-based formulation and tumbling inherent to the background flows [49]. To extract meaningful data, we further post-process the $F$, $S_2$, $E$ curves by taking their time average over the interval $t \in [0, T]$.

### A. Strain and alignment

The plots reveal highly distinct material responses from each phase. Figures 3(a) and (b) show the time-averaged strain $\frac{1}{T}\int_0^T E \, \mathrm{d}t$ over a broad range of shear rates. Strain $E$ measures the non-rigid-body deformation relative to the initial state and expectedly increases with shear rate. The greatest increase occurs with the Type I amphiphiles, suggesting that this phase has the lowest elastic modulus (squares). In comparison, the striated phase consisting of Type III polar JP is basically rigid (triangles).

Figures 3(c) and (d) plot the time-averaged alignment order $S_2$. The vesicle and striated phases possess the greatest alignment order and, for the most part, $S_2$ decreases with increases in shear rate. But there is an exception. The Type I bilayer phase alignment order actually increases under both shear and TG flows (solid squares). This suggests that the mixing action of background flow has the effect of moving the disordered bilayer phase out of a local equilibrium and into a state with greater order. This surprising increase, brought about by combining previously broken bilayer end caps, is accompanied by a slight decrease in free energy (Figure 4(a), solid squares).

The sudden jumps in Figures 3(a) and (b) and commensurate drops in panels (c) and (d) indicate the existence of a critical shear rate $\dot{\gamma}_*$. This means that for $\dot{\gamma} < \dot{\gamma}_*$, the JP phase remains intact while for $\dot{\gamma} > \dot{\gamma}_*$, the phase ruptures. For example, the vesicle BL phase has $\dot{\gamma}_*$ approximately $0.05 \ \mathrm{ns}^{-1}$ under shear flow and TG flow. However, the critical shear rate is flow-pattern dependent because the striated phase has $\dot{\gamma}_* = 0.14 \ \mathrm{ns}^{-1}$ under shear flow while $\dot{\gamma}_* = 0.05 \ \mathrm{ns}^{-1}$ under TG flow. Due to variable stress distribution, the critical shear rate in TG flow likely depends on the cell size parameter $\lambda$. The disordered bilayer phase does not really possess a critical shear rate because it already consists of several, disjoint components. The jump in Figure 3(a) (solid squares) simply corresponds to disjoint components drifting apart in the shear flow. The Type II multilamellar phase did not rupture for any of the shear rates considered.

### B. Free energy

Figure 4 plots the time-averaged relative free energy $\frac{1}{T}\int_0^T (F - F_0) \, \mathrm{d}t$ where $F_0$ is (19) at $t = 0$. The greatest increase occurs with the Type II multilamellar phase, with the other phases showing a moderate change in a few $\mathrm{k_B T \, nm^{-1}}$.

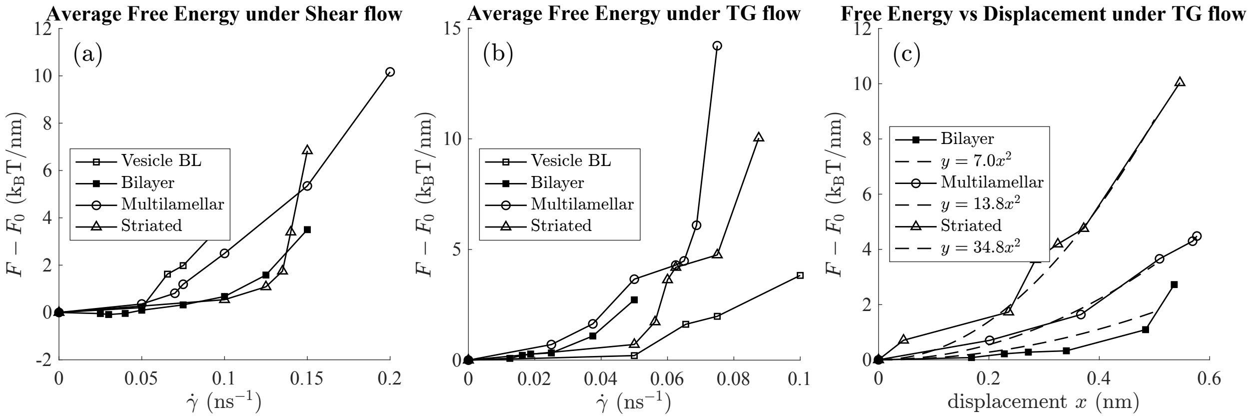


FIG. 4. The change of average free energy versus shear rates for shear flow and TG flow simulation results are plotted in panels (a)-(b). Panel (c) contains quadratic fits to the change in free energy as a function of displacement in interparticle distance from equilibrium.

Figure 4(c) plots the free energy against the displacement $x = cE$ representing the change in mean interparticle displacement from equilibrium; $c = 1.25$ nm is the particle radius. The energies in Figure 4(c) are essentially quadratic in $x$ suggesting that the interactions are harmonic locally around equilibrium. The harmonic bond strength is strongest between polar JP, and greater by a factor of two and five than that for asymmetric hydrophobes and amphiphiles, respectively. This makes sense when considering that the free energy of the steady-state striated phase is also greatest (Figure 2(c), around 85 $\mathrm{k_B T\ nm^{-1}}$). However, the bond strength in the multilamellar phase comes in second, despite having least steady-state free energy (around 15 $\mathrm{k_B T\ nm^{-1}}$). The data point to the fact that the binding properties do not merely scale with free energy, but also involve the details of the interface's hydrophobicity which are tuned by (18) in our model.

### C. Rheology

So far, we have considered static material properties, namely constant strains maintained by an external force provided by background flow. Now we consider dynamic material properties. Specifically, we look at the strain rate

$$\dot{E} = \left( \frac{1}{T} \int_0^T \left| \frac{dE}{dt} \right|^2 \mathrm{d}t \right)^{1/2} . \tag{26}$$

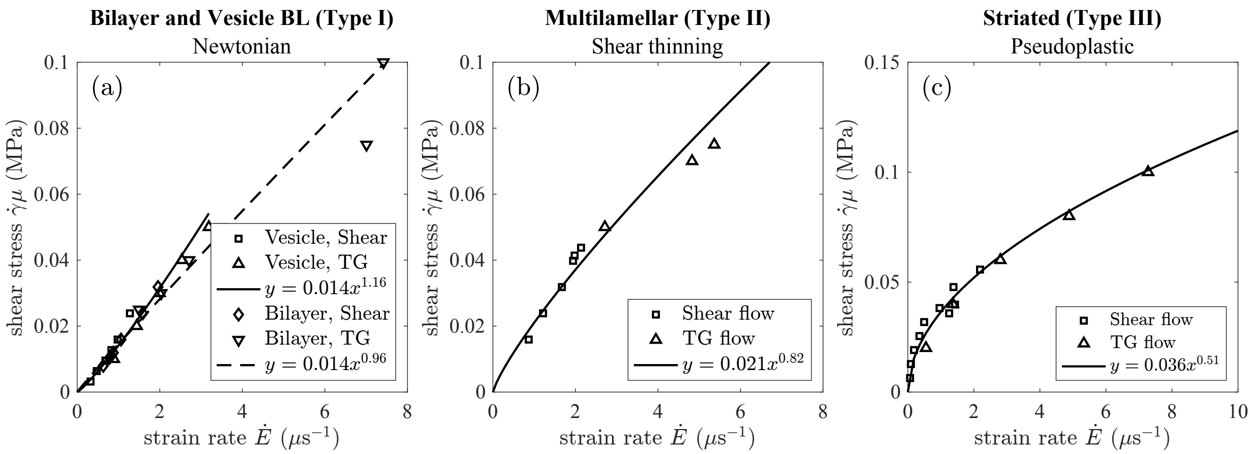


FIG. 5. Rheology of Type I, II, and III phases. Panel (a) shows that bilayer phases behave as a Newtonian fluid. Panel (b) provides that the multilamellar phase shows a near shear thinning behaviour. A pseudoplastic behaviour of deformation in striated phases is shown in panel (c).

The reason for defining $\dot{E}$ in this way is that the shear flow $\mathbf{u}_\infty^{\mathrm{sh}}$ simulations correspond to a complex fluid within a drag plate rheometer where the shear stress is set by $\mu\dot{\gamma}$ and the observed, sample shear rate is $\dot{E}$. The definitions carry over to the TG flow case directly. Also, as a practical consideration, the rotation of non-isotropic JP phases in the background flow leads to oscillation in the strain time courses making systematic fitting challenging (see Supplementary Material Figures S1–S8 [49]). The integral in (26) averages out these oscillations and gives physically meaningful values.

The shear stress-strain rate data are excellently fit by power laws. Figures 5(a)–(c) show the data for Type I, Type II and Type III JPs, respectively, under both shear flow (squares) and TG flow (triangles). The bilayer phases consisting of Type I JPs are basically Newtonian with viscosity 0.014 MPa µs = 14 mPa s, about 14 times the viscosity of water at room temperature (Figures 5(a), dashed curve). The vesicle bilayer phase is slightly shear thickening (Figure 5(a), solid curve). Similar shear thickening behaviors are found in continuum vesicle models [53, 54]. The multilamellar phase consisting of Type II JPs is somewhat shear thinning, but its viscosity is larger than for Type I. Finally, the striated phase is strongly shear-thinning. This further explains the rigid-like behavior of the striated phase found in the strain, shear-rate relationships from Figures 3(a) and (b) (triangles).

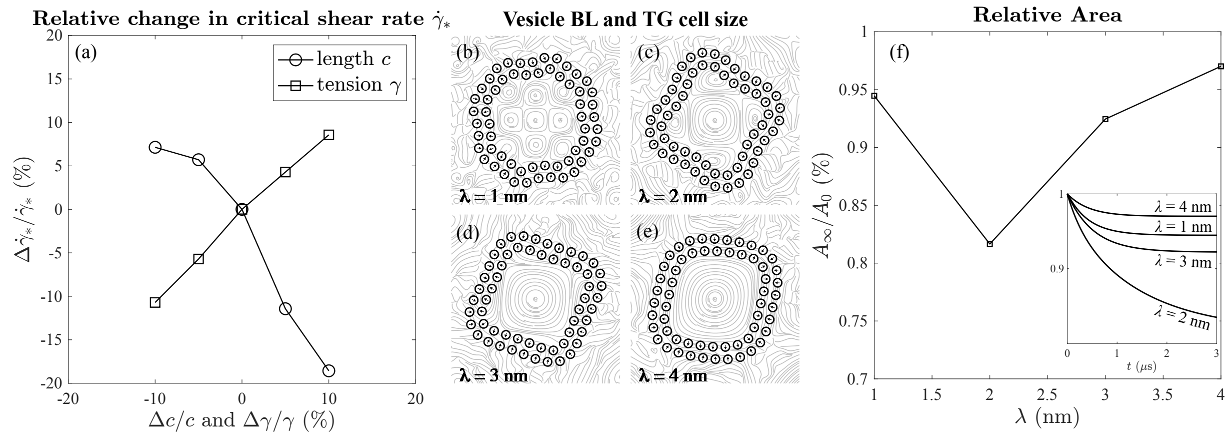


FIG. 6. In panel (a), the relative change in $\dot{\gamma}_*$ is linear in the relative change of the tension parameters $\gamma$ and $M$ with slope 1. Additionally, the relative change in $\dot{\gamma}_*$ has slope $-2$ with respect to the relative change in the length parameters $c$, $\rho$, and $\rho_0$. Panels (b)–(e) show the tank-treading configuration of a vesicle bilayer the configurations with streamlines of a vesicle is in a TG flow at $t = 1$ μs with $\lambda = 1, 2, 3, 4$, respectively. In panel (f), inset, the relative enclosed area $A/A_0$ for the four cases in panels (b)–(e) decays to a steady state. The steady-state $A_\infty/A_0$ relative area is non-monotonic in $\lambda$.

### D. Discussion

We choose the range of shear rates $\dot{\gamma} \in [0, 0.02]$ ns$^{-1}$ by analyzing the capillary number of the JP phases. With this range, there is a critical shear rate $\dot{\gamma}_*$ for the vesicle BL and striated phases where shear stresses exceeded elastic stresses, leading to rupture. The multilamellar phase did not rupture. By varying model parameters, we perform a dimensional analysis on $\dot{\gamma}_*$. Focusing on Type III JPs in shear flow, $\dot{\gamma}_* = 0.14$ ns$^{-1}$ for the basic model parameters (see Section III). Increasing and decreasing the tension parameters $\gamma$ and $M$ by up to 10% (collectively denoted $\Delta\gamma/\gamma$) led to basically the same relative increase/decrease in critical shear rate (denoted $\Delta\dot{\gamma}_*/\dot{\gamma}_*$). This suggests that the critical shear rate scales linearly with the tension parameters. Conversely, increasing (resp. decreasing) the length parameters $c$, $\rho$, and $\rho_0$ by up to 10% (collectively denoted $\Delta c/c$) leads to roughly twice the relative decrease (resp. increase) in the critical shear rate. This points to an inverse-quadratic scaling in length. Figure 6(a) summarizes the findings and suggests the scaling

$$\mu\dot{\gamma}_* = K_{\mathrm{III}}\frac{\gamma L}{c^2}. \tag{27}$$

The scalar $K_{\text{III}}$ is specific to the striated phase under shear flow. Here $L$ is the diameter of the phase sample, which is proportional to $\gamma^*$ since the striated phase tends to cleave during rupture (see Supplementary movie [49]). Our previous work [19] found the scaling $\mu\dot{\gamma}_* = K_{\text{I}}\gamma c^2/(\rho L^2)$ for a vesicle BL in shear flow.

The Results section showed that variations in free energy and strain generally depend on the distribution of fluid stresses i.e., shear versus TG flow. To further illustrate how fluid stresses interact with the geometry of the JP phases, we initialize a circular vesicle bilayer in various TG-flow cell sizes $\lambda$ ranging from $\lambda = 1$ nm in Figure 6(b) to $\lambda = 4$ nm in Figure 6(e). These JP vesicles fluctuate and deform around a steady shape of an octagon ($\lambda = 1$ nm), a dimpled square ($\lambda = 2$ nm), a rounded diamond ($\lambda = 3$ nm), and a rounded rectangle ($\lambda = 4$ nm). See Section S1 in the Supplementary Material for a movie showing the dynamics of the JP vesicle for the four different values of $\lambda$ in Figure 6(b)–(e) [49].

For $\lambda = 1$ nm and $\lambda = 2$ nm, multiple TG cells are inside the JP vesicle as the inner leaflet of JPs move clockwise along the boundary faster than the outer leaflet. For $\lambda = 3$ nm and $\lambda = 4$ nm, there is only one TG cell inside the JP vesicle and the JPs in the bilayer tank-tread in the counter-clockwise direction (Figure 6(b)–(e)). Finally, we calculated the vesicle area $A$ and length $L$. As shown in Figure 6(f), the relative area achieves a steady state $A_\infty/A_0$ that is greatest for $\lambda = 4$ nm yet least for $\lambda = 2$ nm. The relative length $L/L_0$, however, is constant in $t$ for all cell sizes (data not shown). In other words, the fluid-structure interactions of JPs give rise to non-monotonic dependence of membrane permeability on the TG cell size $\lambda$. Such dynamic permeability due to fluid-structure interactions is also found in the clogging of spherical particles in a rectangular microfluidic channel [55].

We have excluded thermal fluctuations because they are unresolved in the JP phases we consider. For a tensionless, planar membrane, the Fourier coefficients for the profile height $h(\mathbf{x}) = \sum_{\mathbf{k}} h(\mathbf{k}) e^{i\mathbf{k}\cdot\mathbf{x}}$ satisfy [56]

$$\langle |h(\mathbf{k})|^2 \rangle = \frac{\mathrm{k_B T}}{L_x L_y} \frac{1}{\kappa |\mathbf{k}|^4}, \tag{28}$$

where $\mathbf{x}$ is a point in an $L_x \times L_y$ rectangular membrane patch, $\mathbf{k} = \left(2\pi m/L_x, 2\pi n/L_y\right)$ with $m, n \in \mathbb{Z}$, not both zero, and $\kappa$ is the membrane bending modulus.

To estimate $h(\mathbf{k})$, the $N_b = 60$ JP vesicle in Figure 3(e) has arclength $L_x \approx 50$ nm. Our prior work [18, 19] gave $\kappa \approx 20\ \mathrm{k_B T}$. Since our simulations are two-dimensional, we restrict our attention to transversely invariant fluctuations where $n = 0$. Substituting these values gives

$$\langle |h(\mathbf{k})|^2 \rangle \approx \frac{4\ \mathrm{nm}^3}{L_y} \frac{1}{m^4}, \quad m = \pm 1, \pm 2, \ldots \tag{29}$$

For any moderate transverse depth, say $L_y > 4$ nm, the leading Fourier coefficient has a magnitude less than 1 nm with the remaining coefficients dropping off to zero precipitously. The expected amplitudes coming from thermal fluctuations are therefore negligible compared to particle size. The elastic moduli for the Type II and Type III phases are greater by a factor of two and five, respectively, than for Type I (Figure 4(c)), making thermal fluctuation even more negligible in these cases.

The fact that the fluctuation amplitudes are small is not a consequence of stiffness. Quite the opposite, the value $\kappa = 20\ \mathrm{k_B T}$ agrees with the experimental literature where micron sized vesicles observably fluctuate [57]. Rather, because the wave vector $\mathbf{k}$ is inversely proportional to the characteristic size of $L_x$ and $L_y$, larger energies are required to fluctuate membranes over smaller wavelengths and these energies exceed available thermal energy when the wavelengths approach tens of nanometers as demonstrated above.

The calculated viscosities—14 mPa s for Type I and 21 mPa s for Type II JP phases—are physically reasonable. In two-dimensional dilute suspensions, the Einstein viscosity correction is $1 + 2\phi + 4\phi^2 + O(\phi^3)$, where $\phi \ll 1$ is the volume fraction [58–61]. In Figures 3(e)–(h), the volume fraction is $\phi \approx 0.5$, which would correspond to a effective shear viscosity of 4 mPa s according to Einstein's viscosity correction. Note, however, that since $\phi = 0.5$ is outside of the dilute limit, one expects viscosities ten or more times greater than the viscosity of water [62] and number of analytical and numerical approaches have been successfully applied to these dense suspensions [63].

Further parametric studies are required to differentiate between passive effects and JPs' preferred alignments. For example, the difference between the values 14 mPa s for Type I and 21 mPa s for Type II JPs can be explained by the fact that the multilamellar phase is more tightly packed than the bilayer phase (Figures 3(e)–(h)). Furthermore, it seems that the viscosity, and the tendency toward shear thinning in the case of Type III JPs where viscosity is effectively infinite for low strain rates (Figure 5(c)), is related to particle coordination. That is, a single JP coordinates with: one neighbor in the apposing bilayer for Type I, two neighbors at the tail and head interfaces for Type II, and four neighbors (front, back, left, and right) for Type III.

Scaling laws for the "virial viscosity", the nonhydrodynamic part of the relative viscosity in steady shear, have been determined experimentally [64]. Other simulation studies have investigated the rheology of strain-hardening capsules as a function of membrane inexstensibility using the three-dimensional immersed boundary method [65], studied dilute suspensions of compound particles [66], and shown how shear thickening in systems with widely different particle properties stems arise when adhesion forces bring particles into frictional contact [67]. Within this context, membrane inexinsibility in the case of Type I amphiphiles and adhesion in general can be inferred from the functional relationships between free energy and displacement in Figure 4(c), for example.

For active particles, researchers have obtained analytical expressions for the effective viscosity resulting from the activity of dilute swimmers in extensional flows [68] and compared numerical predictions under shear flow derived from Stokesian dynamics and lubrication theory [69]. Suspensions of pushers can yield an apparent reduction in viscous dissipation arising from particle activity In contrast, the JP suspensions of the present study do not inject, but rather store energy coming from the background flow.

## VI. CONCLUSION

In this work, we employ the newly developed JP model using BIEs [18, 19] and tune the boundary conditions with energy normalization to study the collective dynamics of amphiphilic (Type I), biased hydrophobic (Type II), and bipolar (Type III) JPs under various flowing conditions (quiescent flow, linear shear flow, and Taylor-Green flow). Three quantities are computed to characterize the dynamics of the collective configurations of JPs: free energy $F$, strain parameter $E$, and scalar order parameter $S_2$. Under a given flow, we use these three measures of deformations to quantify the differences in the collective dynamics between the three types of JPs. These results, summarized below, provide general insight into the dynamic control of active particles in a viscous suspension.

In a quiescent flow, the free energy profiles demonstrate that the relaxation process for particles confined in a certain size of box is independent of the number of particles. However, we find that the final configurations does depend on the initial distribution of particle directors $\mathbf{d}_i$. Therefore, multiple patterns or local energy minimum states may appear depending on the initial setup.

Under a relatively weak linear shear flow, the amphiphilic JPs behave as a unilamellar vesicle that elongates and tank-treads, with the scalar order parameter increasing over time. The assembly of multilamellar and striated JP structures resemble a rigid body motion with minimal deformation.

The effective viscosity of the material quantitatively validates this result. High shear-rate cases provide a range of critical shear rates where the structures break apart and undergo topological changes. We further show that free energy, scalar order parameter, and strain are effective measures to quantitatively capture the collective hydrodynamics of JPs under a linear shear flow.

Under a Taylor-Green flow, the amphiphilic JPs are the most interesting, exhibiting different vesicle shapes depending on the ratio of the size of the TG flow to the vesicle size. These results show that the shape of the vesicle, whether square or polygonal, can be controlled by adjusting the size of the cell in the TG flow. In addition the permeability of the JP bilayer varies non-monotonically with the TG cell size. On the other hand, the assembly of multilamellar JPs and the striated JPs behave more like a rigid body with connected subdomains, and the number of subdomains increases with increasing strength of the TG flow. Overall, the multilamellar (Type II) JP assembly behaves as a shear-thinning fluid, while the striated (Type III) JP assembly possesses a yield stress.

The results reported here provide an inroad modeling framework for hydrodynamics of active colloids [3, 14, 70, 71]. The present study also helps to understand the rheology of JP oligomers that may be realized in experiments. We are extending this study to three dimensional systems with more realistic features such as size distributions of JPs and thermal fluctuations [36]. From a numerical perspective, it is straightforward to include random perturbations in the particle shape and boundary condition that mimic interfacial properties found in lab conditions [4, 10, 11, 17].

## VII. APPENDIX

The boundary integral calculation of (19) relies on the following identity

$$\nabla u(\mathbf{x}) \cdot \boldsymbol{\nu}_{\mathbf{x}} = -\frac{1}{\rho^2}\mathbf{t}_{\mathbf{x}} \cdot \mathcal{S}[\sigma \mathbf{t}](\mathbf{x}) + \frac{\mathrm{d}}{\mathrm{d}s}\mathcal{S}\left[\frac{\mathrm{d}\sigma}{\mathrm{d}s}\right](\mathbf{x}), \quad \mathbf{x} \in \partial\Omega. \tag{30}$$

Here, $\mathbf{t}_{\mathbf{x}}$ is the tangent vector and $\mathrm{d}/\mathrm{d}s$ is the arclength derivative. Substituting (30) into (19) for the normal derivative leads to the single layer, $\mathcal{S}$, which is more straightforward to evaluate. The arclength derivative is computed using the spectrally accurate Fourier differentiation.

To prove (30), let

$$\mathcal{S}[\sigma](\mathbf{x}) = \int_{\partial\Omega} G(\mathbf{x}-\mathbf{y})\sigma(\mathbf{y})\ \mathrm{d}s_{\mathbf{y}} \tag{31}$$

be the single layer potential for a density function $\sigma$. Fix $\mathbf{x} \in \partial\Omega$, let $\boldsymbol{\nu}_{\mathbf{x}}$ and $\boldsymbol{\nu}_{\mathbf{y}}$ be the unit normal at $\mathbf{x}$, respectively $\mathbf{y}$, in $\partial\Omega$, and let $\mathbf{z} \in \Omega$. The subscripts in $\nabla_{\mathbf{z}}$ and $\nabla_{\mathbf{y}}$ denote differentiation with respect to $\mathbf{z}$, respectively $\mathbf{y}$.

Recall from (11) that $u = \mathcal{D}[\sigma]$. Then

$$\begin{aligned}\nabla_{\mathbf{z}} u(\mathbf{z}) \cdot \boldsymbol{\nu}_{\mathbf{x}} &= \boldsymbol{\nu}_{\mathbf{x}} \cdot \nabla_{\mathbf{z}} \int_{\partial\Omega} \frac{\partial G(\mathbf{z}-\mathbf{y})}{\partial \boldsymbol{\nu}_{\mathbf{y}}} \sigma(\mathbf{y}) \, \mathrm{d}s_{\mathbf{y}} \\ &= \int_{\partial\Omega} \boldsymbol{\nu}_{\mathbf{x}}^{\top} \left( \nabla_{\mathbf{z}} \nabla_{\mathbf{y}}^{\top} G(\mathbf{z}-\mathbf{y}) \right) \boldsymbol{\nu}_{\mathbf{y}} \sigma(\mathbf{y}) \, \mathrm{d}s_{\mathbf{y}} \\ &= -\int_{\partial\Omega} \boldsymbol{\nu}_{\mathbf{x}}^{\top} \left( \nabla_{\mathbf{y}} \nabla_{\mathbf{y}}^{\top} G(\mathbf{z}-\mathbf{y}) \right) \boldsymbol{\nu}_{\mathbf{y}} \sigma(\mathbf{y}) \, \mathrm{d}s_{\mathbf{y}},\end{aligned}$$

since we can interchange $\nabla_{\mathbf{z}}$ with $-\nabla_{\mathbf{y}}$. Following Hsiao and Wendland [37] (see §1.2),

$$\boldsymbol{\nu}_{\mathbf{x}}^{\top} \left( \nabla_{\mathbf{y}} \nabla_{\mathbf{y}}^{\top} G(\mathbf{z}-\mathbf{y}) \right) \boldsymbol{\nu}_{\mathbf{y}} = -\mathbf{t}_{\mathbf{x}}^{\top} \left( \nabla_{\mathbf{y}} \nabla_{\mathbf{y}}^{\top} G(\mathbf{z}-\mathbf{y}) \right) \mathbf{t}_{\mathbf{y}} + \Delta_{\mathbf{y}} G(\mathbf{z}-\mathbf{y}) \mathbf{t}_{\mathbf{x}} \cdot \mathbf{t}_{\mathbf{y}}. \tag{32}$$

Then, using that $\Delta_{\mathbf{y}} G(\mathbf{z}-\mathbf{y}) = \rho^{-2} G(\mathbf{z}-\mathbf{y})$, interchanging $\nabla_{\mathbf{y}}$ with $-\nabla_{\mathbf{z}}$ once more, and integrating by parts in arclength $s$, we obtain

$$\begin{aligned}\nabla_{\mathbf{z}} u(\mathbf{z}) \cdot \boldsymbol{\nu}_{\mathbf{x}} &= -\int_{\partial\Omega} \Delta_{\mathbf{y}} G(\mathbf{z}-\mathbf{y}) \mathbf{t}_{\mathbf{x}} \cdot \mathbf{t}_{\mathbf{y}} \sigma(\mathbf{y}) \, \mathrm{d}s_{\mathbf{y}} + \int_{\partial\Omega} (\mathbf{t}_{\mathbf{x}} \cdot \nabla_{\mathbf{y}})(\mathbf{t}_{\mathbf{y}} \cdot \nabla_{\mathbf{y}} G(\mathbf{z}-\mathbf{y})) \sigma(\mathbf{y}) \, \mathrm{d}s_{\mathbf{y}} \\ &= -\int_{\partial\Omega} \frac{1}{\rho^2} G(\mathbf{z}-\mathbf{y}) \mathbf{t}_{\mathbf{x}} \cdot \mathbf{t}_{\mathbf{y}} \sigma(\mathbf{y}) \, \mathrm{d}s_{\mathbf{y}} - (\mathbf{t}_{\mathbf{x}} \cdot \nabla_{\mathbf{z}}) \int_{\partial\Omega} \frac{\mathrm{d}}{\mathrm{d}s_{\mathbf{y}}} G(\mathbf{z}-\mathbf{y}) \sigma(\mathbf{y}) \, \mathrm{d}s_{\mathbf{y}} \\ &= -\frac{1}{\rho^2} \mathbf{t}_{\mathbf{x}} \cdot \int_{\partial\Omega} G(\mathbf{z}-\mathbf{y}) \mathbf{t}_{\mathbf{y}} \sigma(\mathbf{y}) \, \mathrm{d}s_{\mathbf{y}} + (\mathbf{t}_{\mathbf{x}} \cdot \nabla_{\mathbf{z}}) \int_{\partial\Omega} G(\mathbf{z}-\mathbf{y}) \frac{\mathrm{d}}{\mathrm{d}s} \sigma(\mathbf{y}) \, \mathrm{d}s_{\mathbf{y}}.\end{aligned}$$

Letting $\mathbf{z} \to \mathbf{x} \in \partial\Omega$, and noting that both sides of the equation are continuous, we obtain (30).

## ACKNOWLEDGMENTS

We thank the anonymous referees for pointing out the Péclet number, capillary number, and fluctuation analysis. E. Corona, M. Rachh, S. Jiang, and T. Beck provided useful insights. B.Q. acknowledges support from the Simons Foundation, Mathematics and Physical Sciences-Collaboration Grants for Mathematicians, Award No. 527139. Y.-N.Y. acknowledges support from NSF (Grants No. DMS 1614863 and No. DMS 195160) and Flatiron Institute, part of Simons Foundation.

---

[1] P. G. de Gennes, Soft matter, Reviews of Modern Physics **64**, 645 (1992).

[2] A. Kirillova, C. Marschelke, and A. Synytska, Hybrid Janus Particles: Challenges and Opportunities for the Design of Active Functional Interfaces and Surfaces, ACS Applied Materials & Interfaces **11**, 9643 (2019).

[3] C. H. Meredith, A. C. Castonguay, Y.-J. Chiu, A. M. Brooks, P. G. Moerman, P. Torab, P. K. Wong, A. Sen, D. Velegol, and L. D. Zarzar, Chemical design of self-propelled Janus droplets, Matter **5**, 616 (2022).

[4] L. C. Bradley, W.-H. Chen, K. J. Stebe, and D. Lee, Janus and patchy colloids at fluid interfaces, Current Opinion in Colloid & Interface Science **30**, 25 (2017).

[5] C. Kang and A. Honciuc, Self-Assembly of Janus Nanoparticles into Transformable Suprastructures, The Journal of Physical Chemistry Letters **9**, 1415 (2018).

[6] L. Hong, A. Cacciuto, E. Luijten, and S. Granick, Clusters of Amphiphilic Colloidal Spheres, Langmuir **24**, 621 (2008).

[7] F. Gheisari, M. Shafiee, M. Abbasi, A. Jangjou, P. Izadpanah, A. Vaez, and A. M. Amani, Janus nanoparticles: an efficient intelligent modern nanostructure for eradicating cancer, Drug Metabolism Reviews **53**, 592 (2021).

[8] Y. Liu, X. Yang, Z. Huang, P. Huang, Y. Zhang, L. Deng, Z. Wang, Z. Zhou, Y. Liu, H. Kalish, N. M. Khachab, X. Chen, and Z. Nie, Magneto-Plasmonic Janus Vesicles for Magnetic Field-Enhanced Photoacoustic and Magnetic Resonance Imaging of Tumors, Angewandte Chemie International Edition **55**, 15297 (2016).

[9] J. Li, J. Wang, Q. Yao, K. Yu, Y. Yan, and J. Zhang, Cooperative Assembly of Janus Particles and Amphiphilic Oligomers: The Role of Janus Balance, Nanoscale **11**, 7221 (2019).

[10] L. C. Bradley, K. J. Stebe, and D. Lee, Clickable Janus Particles, Journal of the American Chemical Society **138**, 11437 (2016).

[11] L. D. Zarzar, V. Sresht, E. M. Sletten, J. A. Kalow, D. Blankschtein, and T. M. Swager, Dynamically reconfigurable complex emulsions via tunable interfacial tensions, Nature **518**, 520 (2015).

[12] M. F. Hagan and G. M. Grason, Equilibrium mechanisms of self-limiting assembly, Reviews of Modern Physics **93**, 025008 (2021).

[13] Y. Collard, G. Grosjean, and N. Vandewalle, Magnetically powered metachronal waves induce locomotion in self-assemblies, Communications Physics **3** (2020).

[14] H. R. Vutukuri, M. Hoore, C. Abaurrea-Velasco, L. van Buren, A. Dutto, T. Auth, D. A. Fedosov, G. Gompper, and J. Vermant, Active particles induce large shape deformations in giant lipid vesicles, Nature **586**, 52 (2020).

[15] F. Boccardo and O. Pierre-Louis, Controlling the Shape of Small Clusters with and without Macroscopic Fields, Physical Review Letters **128**, 256102 (2022).

[16] V. N. Manoharan, Colloidal matter: Packing, geometry, and entropy, Science **349**, 1253751 (2015).

[17] A. Kirillova, G. Stoychev, L. Ionov, and A. Synytska, Self-Assembly Behavior of Hairy Colloidal Particles with Different Architectures: Mixed versus Janus, Langmuir **30**, 12765 (2014).

[18] S.-P. P. Fu, R. Ryham, A. Klöckner, M. Wala, S. Jiang, and Y.-N. Young, Simulation of Multiscale Hydrophobic Lipid Dynamics via Efficient Integral Equation Methods, Multiscale Modeling & Simulation **18**, 79 (2020).

[19] S.-P. Fu, B. Quaife, R. Ryham, and Y.-N. Young, Two-Dimensional Vesicle Hydrodynamics from Hydrophobic Attraction Potential, Journal of Fluid Mechanics **941**, A41 (2022).

[20] J. F. Nagle and S. Tristram-Nagle, Structure of lipid bilayers, Biochimica et Biophysica Acta (BBA) - Reviews on Biomembranes **1469**, 159 (2000).

[21] T. Krüger, S. Frijters, F. Günther, B. Kaoui, and J. Harting, Numerical simulations of complex fluid-fluid interface dynamics, The European Physical Journal Special Topics **222**, 177 (2013).

[22] N. Grandmaison, D. Brancherie, and A.-V. Salsac, Modelling of damage of a liquid-core microcapsule in simple shear flow until rupture, Journal of Fluid Mechanics **914**, A25 (2021).

[23] M. Er-Rafik, K. Ferji, J. Combet, O. Sandre, S. Lecommandoux, M. Schmutz, J.-F. Le Meins, and C. M. Marques, Tear of lipid membranes by nanoparticles, Soft Matter **18**, 3318 (2022).

[24] S. R. Keller and R. Skalak, Motion of a tank-treading ellipsoidal particle in a shear flow, Journal of Fluid Mechanics **120**, 27 (1982).

[25] R. Finken, A. Lamura, U. Seifert, and G. Gompper, Two-dimensional fluctuating vesicles in linear shear flow, The European Physical Journal E **25**, 309 (2008).

[26] H. Zhao and E. S. G. Shaqfeh, The dynamics of a vesicle in simple shear flow, Journal of Fluid Mechanics **674**, 578 (2011).

[27] A. F. Brandner, S. Timr, S. Melchionna, P. Derreumaux, M. Baaden, and F. Sterpone, Modelling lipid systems in fluid with Lattice Boltzmann Molecular Dynamics simulations and hydrodynamics, Scientific Reports **9**, 16450 (2019).

[28] M. Banik, S. Sett, C. Bakli, A. K. Raychaudhuri, S. Chakraborty, and R. Mukherjee, Substrate wettability guided oriented self assembly of Janus particles, Scientific Reports **11**, 1 (2021).

[29] F.-F. Hu, Y.-W. Sun, Y.-L. Zhu, Y.-N. Huang, Z.-W. Li, and Z.-Y. Sun, Enthalpy-driven self-assembly of amphiphilic Janus dendrimers into onion-like vesicles: a Janus particle model, Nanoscale **11**, 17350 (2019).

[30] S. Marčelja, Structural Contribution to Solute-Solute Interaction, Croatica Chemica Acta **49**, 347

(1977).

[31] G. Gompper, M. Hauser, and A. A. Kornyshev, "Confined" water and hydrophobic attraction as a result of metastable coordination, stabilized by hydrophobic surfaces, The Journal of Chemical Physics **101**, 3378 (1994).

[32] J. C. Eriksson, S. Ljunggren, and P. M. Claesson, A phenomenological theory of long-range hydrophobic attraction forces based on a square-gradient variational approach, Journal of the Chemical Society, Faraday Transactions 2: Molecular and Chemical Physics **85**, 163 (1989).

[33] Q. Lin, E. E. Meyer, M. Tadmor, J. N. Israelachvili, and T. L. Kuhl, Measurement of the Long- and Short-Range Hydrophobic Attraction between Surfactant-Coated Surfaces, Langmuir **21**, 251 (2005).

[34] J. N. Israelachvili, S. Marčelja, and R. G. Horn, Physical principles of membrane organization, Quarterly Reviews of Biophysics **13**, 121 (1980).

[35] Q. Hang and Q. Wang, A hybrid phase field method for fluid-structure interactions in viscous fluids, arxiv **2109.07361** (2021).

[36] R. Kohl, E. Corona, V. Cheruvu, and S. Veerapaneni, Fast and accurate solvers for simulating Janus particle suspensions in Stokes flow, arxiv **2104.14068** (2022).

[37] G. C. Hsiao and W. L. Wendland, *Boundary Integral Equations* (Springer Berlin Heidelberg, Berlin, Heidelberg, 2008).

[38] H. Power and G. Miranda, Second kind integral equation formulation of Stokes' flows past a particle of arbitrary shape, SIAM Journal on Applied Mathematics **47**, 689 (1987).

[39] C. Pozrikidis, *Boundary Integral and Singularity Methods for Linearized Viscous Flow* (Cambridge University Press, New York, NY, USA, 1992).

[40] M. Rachh and L. Greengard, Integral equation methods for elastance and mobility problems in two dimensions, SIAM Journal on Numerical Analysis **54**, 2889 (2016).

[41] E. Corona, L. Greengard, M. Rachh, and S. Veerapaneni, An integral equation formulation for rigid bodies in Stokes flow in three dimensions, Journal of Computational Physics **332**, 504 (2017).

[42] B. Quaife and G. Biros, High-volume fraction simulations of two-dimensional vesicle suspensions, Journal of Computational Physics **274**, 245 (2014).

[43] D. Boal, *Mechanics of the Cell Second Edition* (Cambridge University Press, Cambridge, United Kingdom, 2012).

[44] P. I. Kuzmin, S. A. Akimov, Y. A. Chizmadzhev, J. Zimmerberg, and F. S. Cohen, Line Tension and Interaction Energies of Membrane Rafts Calculated from Lipid Splay and Tilt, Biophysical Journal **88**,

1120 (2005).

[45] A. D. Petelska, Interfacial tension of bilayer lipid membranes, Central European Journal of Chemistry **10**, 16 (2012).

[46] M. B. Jackson, The Hydrophobic Effect in Solute Partitioning and Interfacial Tension, Scientific Reports **6**, 6 (2016).

[47] A. J. García-Sáez, S. Chiantia, and P. Schwille, Effect of Line Tension on the Lateral Organization of Lipid Membranes, Journal of Biological Chemistry **282**, 33537 (2007).

[48] S. Marčelja and N. Radic, Repulsion of interfaces due to boundary water, Chemical Physical Letters **42**, 129 (1976).

[49] See Supplemental Material at [link will be inserted by publisher] for movies showing the transition of 60 JPs that are initialized randomly to the steady state configurationsa and the dynamics of the JP suspensions. Supplementary materials also contain figures of the fully resolved simulation time-courses organized in terms of the bilayer, vesicle BL, multilamellar, and striated JP configurations under shear flow and under TG flow.

[50] J. V. Selinger, *Introduction to the Theory of Soft Matter: From Ideal Gases to Liquid Crystals* (Springer International Publishing, Switzerland, 2016).

[51] A. L. Bernard, M.-A. Guedeau-Boudeville, V. Marchi-Artzner, T. Gulik-Krzywicki, J.-M. D. Meglio, and L. Jullien, Shear-induced permeation and fusion of lipid vesicles, Journal of Colloid and Interface Science **287 1**, 298 (2005).

[52] Y.-I. Cho and D. J. Cho, Hemorheology and Microvascular Disorders, Korean Circulation Journal **41**, 287 (2011).

[53] A. Rahimian, S. K. Veerapaneni, and G. Biros, Dynamic simulation of locally inextensible vesicles suspended in an arbitrary two-dimensional domain, a boundary integral method, Journal of Computational Physics **229**, 6466 (2010).

[54] A. Nait-Ouhra, A. Farutin, H. Ez-zahraouy, A. Benyoussef, and C. Misbah, Rheology of a confined vesicle suspension, Physical Review Fluids **4**, 103602 (2019).

[55] C. P. Moore, J. Husson, A. Boudaoud, G. Amselem, and C. N. Baroud, Clogging of a rectangular slit by a spherical soft particle, Phys. Rev. Lett. **130**, 064001 (2023).

[56] R.-J. C. Merath and U. Seifert, Fluctuation spectra of free and supported membrane pairs, The European Physical Journal E **23**, 103 (2006).

[57] H. A. Faizi, C. J. Reeves, V. N. Georgiev, P. M. Vlahovska, and R. Dimova, Fluctuation spectroscopy of

giant unilamellar vesicles using confocal and phase contrast microscopy, Soft Matter **16**, 8996 (2020).

[58] V. Doyeux, S. Priem, L. Jibuti, A. Farutin, M. Ismail, and P. Peyla, Effective viscosity of two-dimensional suspensions: Confinement effects, Physical Review Fluids **1**, 043301 (2016).

[59] B. M. Haines and A. L. Mazzucato, A Proof of Einstein's Effective Viscosity for a Dilute Suspension of Spheres, SIAM Journal on Mathematical Analysis **44**, 2120 (2011).

[60] A. S. Khair, The 'Einstein correction' to the bulk viscosity in n dimensions, Journal of Colloid and Interface Science **302 2**, 702 (2006).

[61] J. F. Brady, The Einstein viscosity correction in *n* dimensions, International Journal of Multiphase Flow **10**, 113 (1983).

[62] B. J. Konijn, O. Sanderink, and N. P. Kruyt, Experimental study of the viscosity of suspensions: Effect of solid fraction, particle size and suspending liquid, Powder Technology **266**, 61 (2014).

[63] É. Guazzelli and O. Pouliquen, Rheology of dense granular suspensions, Journal of Fluid Mechanics **852** (2018).

[64] J. J. J. Gillissen, A. Papadopoulou, S. Balabani, M. K. Tiwari, and H. J. Wilson, Suspension rheology of adhesive particles at high shear-rates, Physical Review Fluids **5**, 053302 (2020).

[65] O. Aouane, A. Scagliarini, and J. Harting, Structure and rheology of suspensions of spherical strain-hardening capsules, Journal of Fluid Mechanics **911**, A11 (2021).

[66] P. K. Singeetham, K. V. S. Chaithanya, and S. P. Thampi, Dilute dispersion of compound particles: deformation dynamics and rheology, Journal of Fluid Mechanics **917**, A2 (2021).

[67] A. Singh, G. L. Jackson, M. van der Naald, J. J. de Pablo, and H. M. Jaeger, Stress-activated constraints in dense suspension rheology, Physical Review Fluids **7**, 054302 (2022).

[68] D. Saintillan, Extensional rheology of active suspensions, Physical Review E **81**, 056307 (2010).

[69] T. Ishikawa, D. Brumley, and T. Pedley, Rheology of a concentrated suspension of spherical squirmers: monolayer in simple shear flow, Journal of Fluid Mechanics **914**, A26 (2021).

[70] A. McGlasson and L. C. Bradley, Investigating Time-Dependent Active Motion of Janus Micromotors using Dynamic Light Scattering, Small **17**, 2104926 (2021).

[71] S. A. Mallory, F. Alarcon, A. Cacciuto, and C. Valeriani, Self-assembly of active amphiphilic Janus particles, New Journal of Physics **19**, 125014 (2017).

# Supplementary Material

# Effects of Tunable Hydrophobicity on the Collective Hydrodynamics of Janus Particles under Flows

Szu-Pei Fu[1,*], Rolf Ryham[2], Bryan Quaife[3] and Y.-N. Young[4],

[1]Department of Mathematics, Trinity College, Hartford, Connecticut 06106, USA

[2]Department of Mathematics, Fordham University, Bronx, NY, USA

[3]Department of Scientific Computing, Florida State University, Tallahassee, Florida 32306, USA

[4]Department of Mathematical Sciences, New Jersey Institute of Technology, Newark, NJ 07102 USA

[*]Corresponding author. Address: Department of Mathematics, Trinity College, 300 Summit Street, Hartford, CT 06106. email: peter.fu@trincoll.edu

### S1. MOVIE DESCRIPTIONS

We consider suspensions of JPs of radius 1.25 nm. The time step size for all simulations is $\Delta t = 0.2$ ns. The colors of the JPs are as follows: for Type I and Vesicles, red is hydrophobic ($\max g > 0$) and blue is hydrophilic ($\min g = 0$); for Type II, red is more hydrophobic ($\max g > 0$) than blue ($\min g > 0$); for Type III, red is positively charged ($\max g > 0$) and blue is negatively charged ($\min g < 0$).

**Relaxation**: The relaxation of 60 circular JPs that are initialized with random locations and orientations. The JPs self-assemble into unilamellar (Type I), multilamellar (Type II), and striated (Type III) configurations. The final configurations are used as initial conditions for the simulations that include a background flow.

**Structures in a Weak Shear Flow**: The relaxed configurations of the 60 JPs are subjected to a weak shear flow. The shear rate is $\dot{\gamma} = 0.05$ ns$^{-1}$ for the Vesicle, Type I, and Type II configurations, and $\dot{\gamma} = 0.1$ ns$^{-1}$ for the Type III configuration. The vesicle undergoes tank-treading and the bilayer increases its orientational order. The multilamellar configuration resembles a rigid body motion, and the striated configuration has an even stronger resemblance to a rigid body motion. No ruptures occur in these examples. The frame rate for the movie of Type I configuration is twice as much ones used in movies of other configurations.

**Structures in a Weak Taylor-Green Flow**: The relaxed configurations of the 60 JPs are subjected to a weak Taylor-Green flow. The flow rate is $\dot{\gamma} = 0.05$ ns$^{-1}$ for the Vesicle, Type I, and Type II configurations, and $\dot{\gamma} = 0.1$ ns$^{-1}$ for the Type III configuration. The vesicle stays intact, whereas the bilayer is pulled apart into different TG cells. Like in the weak shear flow example, the multilamellar and striated configurations behave as rigid bodies.

**Structures in a Strong Shear Flow**: The relaxed configurations of the 60 JPs are subjected to a strong shear flow. The shear rate is $\dot{\gamma} = 0.075$ ns$^{-1}$ for the Vesicle configuration, $\dot{\gamma} = 0.1$ ns$^{-1}$ for the Type I configuration, and $\dot{\gamma} = 0.15$ ns$^{-1}$ for the Type II and Type III configurations. In all cases, the structure is ruptured by the flow. The frames are stabilized by moving with the center of mass of all the JPs.

**Structures in a Strong Taylor-Green Flow**: The relaxed configurations of the 60 JPs are subjected to a strong Taylor-Green flow. The flow rate is $\dot{\gamma} = 0.1$ ns$^{-1}$ for the Vesicle, Type I, and Type II configurations, and $\dot{\gamma} = 0.15$ ns$^{-1}$ for the Type III configuration. In all cases, the structure is ruptured by the flow and there is a significant reduction in the orientation order. While the Vesicle Type I configurations are broken into several pieces, the main body of the Type II and Type III configurations are not pulled apart by the background flow.

**JP Vesicle in Various Taylor-Green Flows**: A circular vesicle bilayer is placed in a Taylor-Green flow. The parameter $\lambda$ controls the TG cell size and the values are varied from 1 nm to 4 nm while the flow rate is chosen so that $\lambda\dot{\gamma} = 0.1$ nm/ns. The parameter $\lambda$ determines the steady-state polygonal tank-treading shape. The rotation direction is clockwise for $\lambda = 1$ nm and $\lambda = 2$ nm, and counterclockwise for $\lambda = 3$ nm and $\lambda = 4$ nm. Streamlines of the flow are included.

## S2. RAW DATA

The following figures plot the fully resolved simulation time-courses organized in terms of the bilayer, vesicle BL, multilamellar, and striated JP configurations under shear flow (Supplementary Figures S1–S4) and under TG flow (Supplementary Figures S5–S8). Throughout, panels (a) are for relative free energy $F - F_0$, panels (b) are for alignment $S_2$, and panels (c) are for strain $E$ (as a percentage). The same vertical and horizontal axes are used for each of the respective panels to facilitate comparison between data sets.

## Shear Flow cases

### Type I, bilayer phase under shear flow

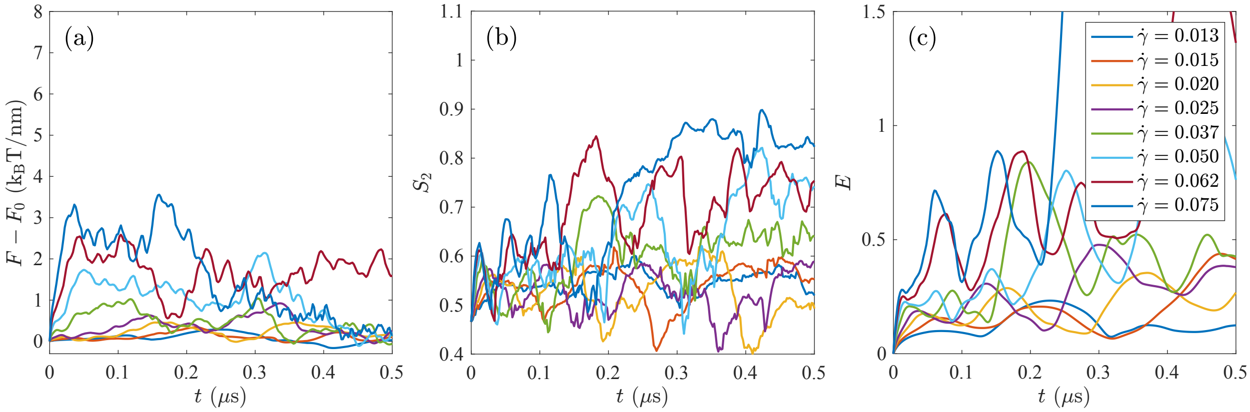


FIG. S1. (a) Relative free energy $F - F_0$, (b) alignment $S_2$, and (c) strain $E$ for Type I, bilayer phase under shear flow with shear rates $\dot{\gamma} = 0.013 - 0.075$ ns$^{-1}$.

### Type I, vesicle BL phase under shear flow

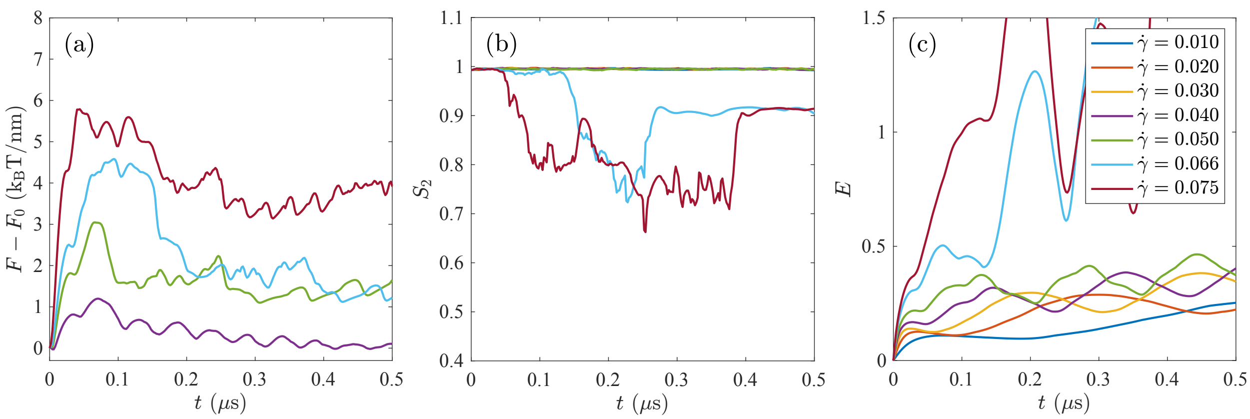


FIG. S2. (a) Relative free energy $F - F_0$, (b) alignment $S_2$, and (c) strain $E$ for Type I, bilayer phase under shear flow with shear rates $\dot{\gamma}$ = 0.01–0.075 ns$^{-1}$. The JP type is the same as Figure S1 except with a vesicle-shaped initial configuration rather than a disordered bilayer.

**Type II, multilamellar phase under shear flow**

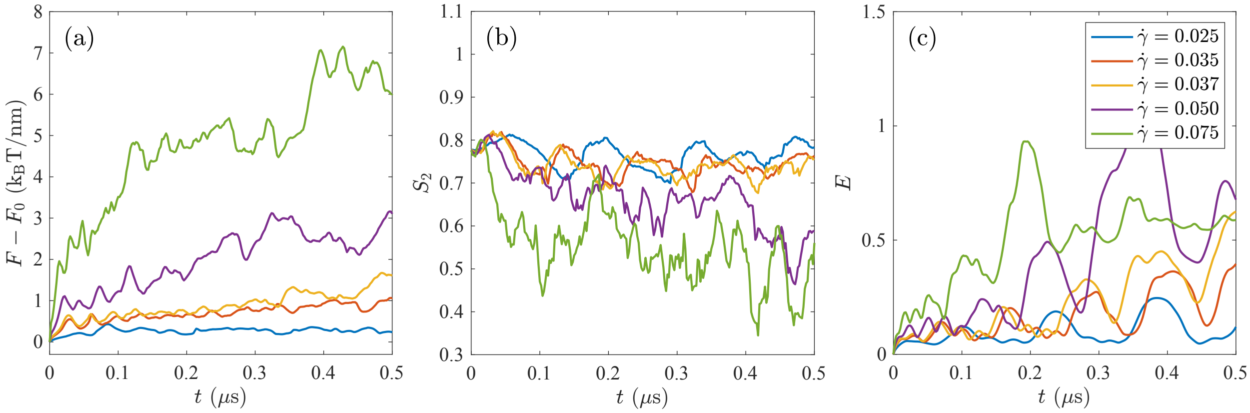


FIG. S3. (a) Relative free energy $F - F_0$, (b) alignment $S_2$, and (c) strain $E$ for Type II, multilamellar phase under shear flow with shear rates $\dot{\gamma} = 0.025$–$0.075$ ns$^{-1}$.

**Type III, striated phase under shear flow**

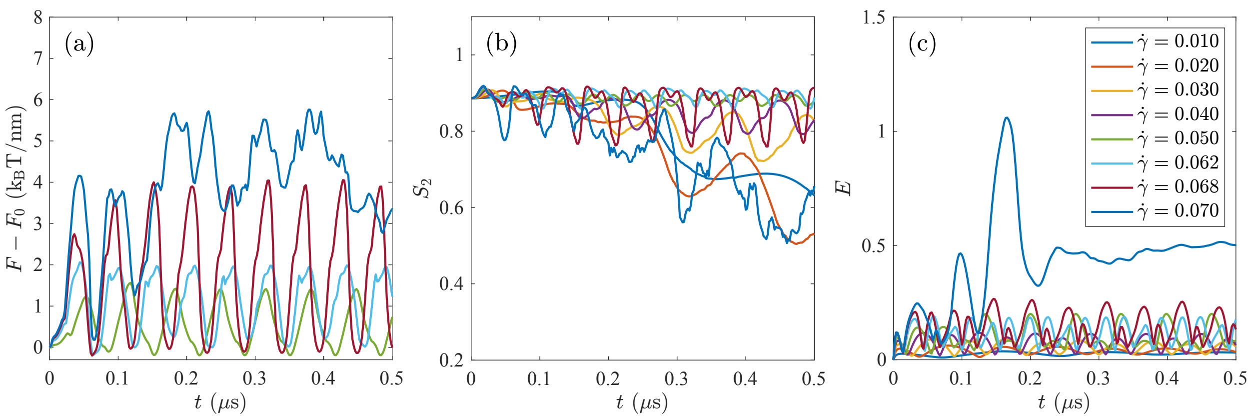


FIG. S4. (a) Relative free energy $F - F_0$, (b) alignment $S_2$, and (c) strain $E$ for Type III, striated phase under shear flow with shear rates $\dot{\gamma} = 0.01$–$0.07$ ns$^{-1}$.

## TG Flow Cases

### Type I, bilayer phase under TG flow

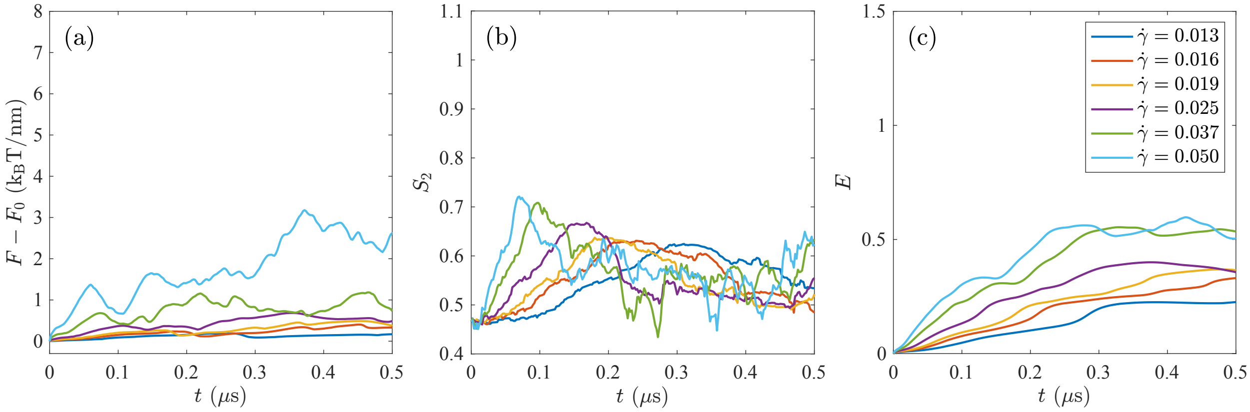


FIG. S5. (a) Relative free energy $F - F_0$, (b) alignment $S_2$, and (c) strain $E$ for Type I, bilayer phase under TG flow with flow rates $\dot{\gamma}$ = 0.013–0.05 ns$^{-1}$.

### Type I, vesicle BL phase under TG flow

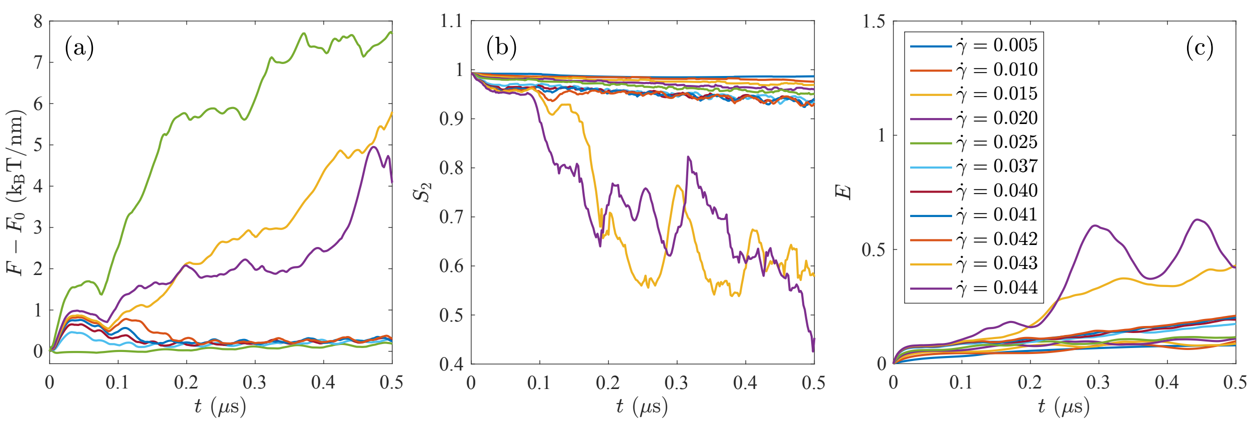


FIG. S6. (a) Relative free energy $F - F_0$, (b) alignment $S_2$, and (c) strain $E$ for Type I, vesicle bilayer phase under TG flow with flow rates $\dot{\gamma}$ = 0.005–0.044 ns$^{-1}$. The JP type is the same as Figure S5 except with a vesicle-shaped initial configuration rather than a disordered bilayer.

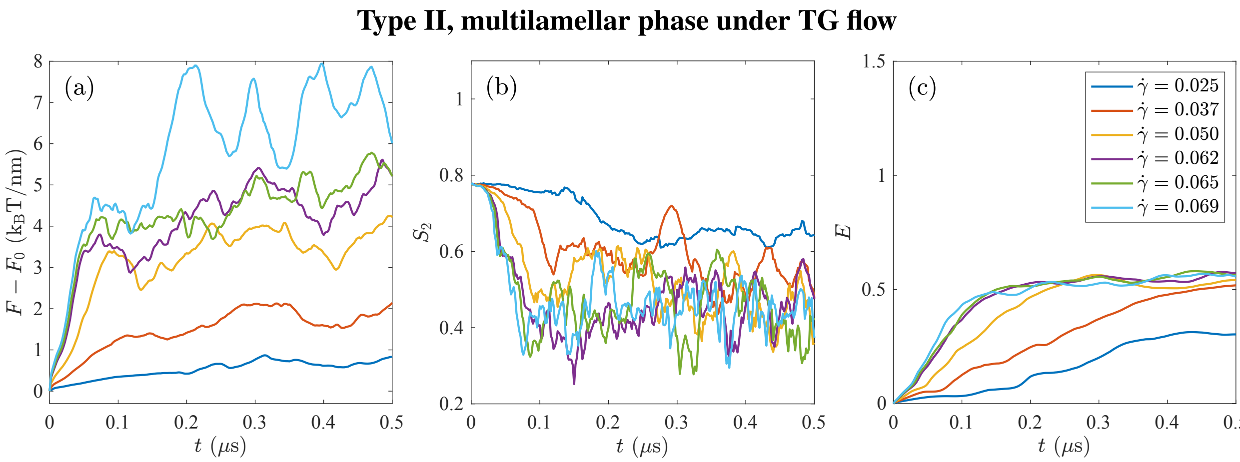


FIG. S7. (a) Relative free energy $F - F_0$, (b) alignment $S_2$, and (c) strain $E$ for Type II, multilamellar phase under TG flow with flow rates $\dot{\gamma} = 0.025$–$0.069$ ns$^{-1}$.

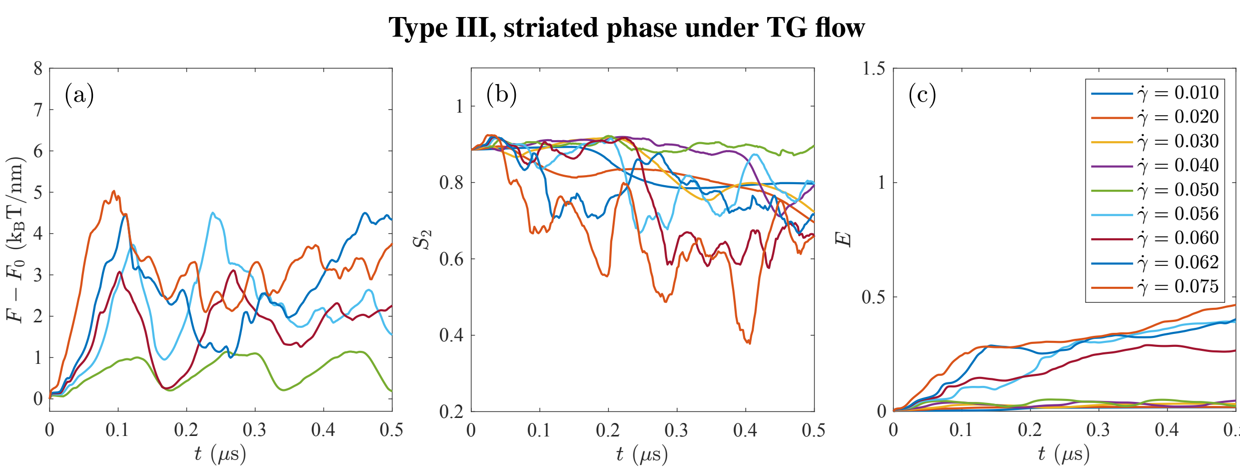


FIG. S8. (a) Relative free energy $F - F_0$, (b) alignment $S_2$, and (c) strain $E$ for Type III, striated phase under TG flow with flow rates $\dot{\gamma} = 0.01$–$0.075$ ns$^{-1}$.